metals

MDPI

Article

Effect of Thermomechanical Treatment on Acicular Ferrite Formation in Ti–Ca Deoxidized Low Carbon Steel

Chao Wang, Xin Wang, Jian Kang, Guo Yuan * and Guodong Wang

The State Key Laboratory of Rolling and Automation, Northeastern University, Shenyang 110819, China; chao_neu@163.com (C.W.); xinwang_research@163.com (X.W.); wwwkangjian@126.com (J.K.); wanggdneu@163.com (G.W.)

* Correspondence: yuanguo@ral.neu.edu.cn; Tel.: +86-024-8368-7220

Received: 12 February 2019; Accepted: 2 March 2019; Published: 6 March 2019



Abstract: Transformation behaviors and mechanical properties under thermomechanical treatment conditions of Ti–Ca deoxidized low carbon steel were studied in comparison to Al–Ca treated steel. A thermomechanical simulation and a hot rolling experiment were carried out. Inclusions and microstructures were characterized, and the transformation mechanism was analyzed. The results indicated that typical inclusions in Ti–Ca deoxidized steel were TiO_x-MnS-Al_2O_3-CaO, TiO_x-MnO-Al_2O_3-CaO, and TiO_x-MnS, which were effective for acicular ferrite (AF) nucleation. Acicular ferrite formation temperature decreased with an increase in cooling rate. A fine AF dominant microstructure was formed under a high driving force for the transformation from austenite to ferrite at lower temperatures. A high deformation of 43–65% discouraged the formation of acicular ferrite because of the increase in austenite grain boundaries serving as nucleation sites. The fraction of high-angled grain boundaries that acted as obstacles to cleavage cracks was the highest in the sample cooled at 5 °C/s because of full AF structure formation. The hardness increased significantly as the cooling rate increased from 2 to 15 °C/s, whereas it decreased under the condition of deformation because of the formation of (quasi-)polygonal ferrite. By applying accelerated water cooling, the mechanical properties, particularly impact toughness, were significantly improved as a result of fine AF microstructure formation.

Keywords: low carbon steel; Ti–Ca oxide; acicular ferrite; thermomechanical treatment; hot deformation; cooling rate

1. Introduction

Intragranular acicular ferrite (AF) is a preferred type of microstructure that has great potential for improving steel strength and toughness because of its relatively high dislocation density, fine-grained structure, and ability in arresting cleavage crack propagation. In order to make use of the advantage, the concept of oxides metallurgy was proposed three decades ago [1] and focused on introducing particular nonmetallic inclusions in steel to promote AF transformation in welding heat-affected zones. Thereafter, oxide metallurgy technology was widely considered and researched. There have been many reported inclusion types effective for AF nucleation, such as Al-Mg-Zr-O, Ti-Al-Mn-O-S, Ti-Al-O-N, Ti-Mn-Al-Si-O-S-N, Mn-S-V-C-N, etc. [2–6]. Some comprehensive reviews were made on the influence of inclusion composition on AF formation potency [7–9], in which Ti- and Mn-containing complex inclusions were described as particularly effective nucleating sites.

Among the research relating inclusion-induced AF nucleation, effective particles have mainly been obtained by means of steel melt deoxidization [2,10], adding oxide powder into steel liquid

or by hot pressing [11,12]. Some works have also studied AF transformation during the hot rolling process [10,13]. For the purpose of improving steel performance by AF transformation, the formation of effective inclusions and microstructural evolution behaviors have been two main study points. With respect to inclusion formation, studies have been concentrated on the deoxidation process and inclusion characterization [14,15], while research on microstructure transformation has mainly been carried out under static thermal treatment conditions without deformation processing. At present, the evaluation of the effect of inclusions on steel microstructure and properties under hot rolling and controlled cooling conditions is insufficient. The effects of austenite deformation and the following cooling on inclusion-induced AF nucleation and its influencing mechanism are still unclear.

With this purpose, in this paper, low-carbon steel deoxidized by Ti–Ca was prepared, and different hot deformation and cooling processes were carried out. Microstructure transformation behaviors and mechanical properties were analyzed combining the influence of Ti–Ca oxide inclusions. AF nucleation possible mechanisms are also discussed.

2. Materials and Methods

Two experimental steels were prepared by a 50-kg vacuum induction furnace (Jinzhou Electric Furnace Ltd, Jinzhou, China). The chemical compositions are listed in Table 1. TC# steel was deoxidized with Ti–Ca deoxidant to obtain effective Ti–Ca oxide particles. A small amount of Cr (0.2 wt %) and B (0.001 wt %) was added to promote AF transformation by reducing the proeutectoid ferrite start temperature. AC# steel was provided for comparison and melted referring to commercial 360-MPa-grade Nb-microalloyed high-strength low-alloy (HSLA) steel. AC# steel was killed by Al and Ca-treated, where Al–Ca oxide inclusions were mainly formed. The Ae_3 temperature was calculated by Thermo-Calc software (V2017b, Thermo-Calc Software AB, Solna, Sweden, 2017) with the TCFE9 database. Austenite nonrecrystallization temperature T_{nr} was calculated according to the Boratto formula [16].

Table 1. Chemical compositions (wt %) and critical temperatures of experimental steels.

Steel	C	Si	Mn	Al	Ti	Ca	Nb	N	S	Fe	Ae_3 (°C)	T_{nr} (°C)
TC#	0.07	0.06	1.5	0.01	0.01	0.001	-	0.003	0.006	Bal.	831	911
AC#	0.07	0.05	1.4	0.035	-	0.001	0.038	0.002	0.005	Bal.	839	1034

Thermomechanical processing experiments were carried out through physical simulation and hot rolling. Thermomechanical simulation was conducted on an MMS-200 simulator machine using Φ 8 mm × 15 mm cylinder samples. Samples were austenitized at 1250 °C for 3 minutes and then uniaxially compressed at 1050 °C with a reduction of 43%, where complete austenite recrystallization occurred. Finally, the deformed samples were continuously cooled at different cooling rates, as shown in Figure 1a. Samples without hot deformation were also simulated with the process shown in Figure 1b. In addition, the effects of different deforming parameters, such as deformation degree and strain rate, were considered, as shown in Figure 1c. In the hot rolling experiment, steel blocks were heated at 1250 °C for 20 minutes and then rolled to 12 mm from 80 mm through 7 passes with a final pass temperature of about 1050 °C. The hot steel plates were cooled by two methods: Cooling in air with a cooling rate of about 0.5 °C/s, and water cooling to about 600 °C with a cooling rate of about 15 °C/s and then cooling in air. The rolling and cooling processes are illustrated in Figure 1d.

Characterization and statistics of inclusions were carried out using samples cut from steel ingots. The samples were mechanically polished, and a series of micrographs were taken by a JXA-8530F electron probe microanalyzer (EPMA, JEOL Ltd, Tokyo, Japan). Inclusion number density and size distribution were analyzed using the micrographs of 1000× magnification with the aid of an IPP image processing tool. For each steel sample, more than 50 inclusions were randomly selected and analyzed by the EPMA, where energy dispersive spectroscopy (EDS, INCA 350, Oxford Instruments, Oxford,

UK) were used for composition analysis. Elements distributions in some selected inclusions were analyzed through line scanning by wavelength dispersive spectroscopy (WDS) of the EPMA.

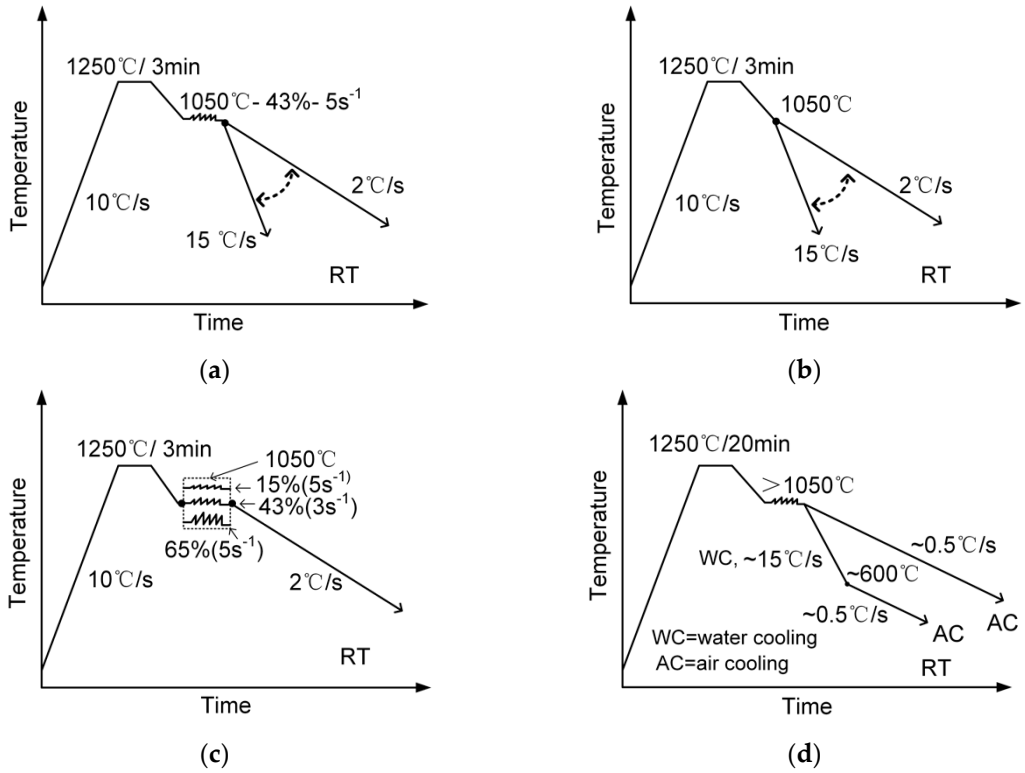


Figure 1. (**a**–**c**) Schematic diagrams of the thermomechanical simulation with different deformation and cooling processes; (**d**) processes of the hot rolling experiment.

Thermomechanical simulation samples and hot-rolled steel samples were etched by 4-vol % nital, and microstructures were observed through a DM2500 M optical microscope (OM, Leica Microsystems, Wetzlar, Germany) and a Ultra-55 scanning electron microscope (SEM, Carl Zeiss, Jena, Germany). Besides, some selected TC# steel samples were electroetched with an 8-vol % perchloric acid solution and used for electron backscattered diffraction (EBSD, Hikari, EDAX-TSL, Draper, UT, USA) analysis by the OIM system with a scanning step size of 0.35 μm. The effects of Ti–Ca oxide particles and thermomechanical conditions on acicular ferrite structure evolution were studied by EBSD.

Tensile samples of dimensions 8 mm in diameter and 40 mm in gauge length were machined from hot-rolled steel plates along the transverse direction. A tensile test was done on a WAW-1000 universal testing machine (Kexin Ltd, Changchun, China) with a tensile speed of 3 mm/min. Charpy v-notch impact samples of dimensions 10 mm × 10 mm × 55 mm were machined along the rolling direction. The impact test was carried out using an Instron 9250 HV Drop Weight Tester (Instron Corporation, Norwood, MA, USA). The Vickers hardness of thermomechanical simulation samples were also tested by a KB hardness testing machine (KB Prüftechnik, Hochdorf-Assenheim, Germany).

3. Results

3.1. Inclusion Characterization

More than 50 fields of view were observed on the polished sample surface by EPMA at a magnification of 1000×. More than 50 inclusions were randomly selected for composition analysis. A typical micrograph is shown in Figure 2a. Inclusions in TC# steel were detected to be mainly Ti-Al-Ca-Mn-O-S type, as shown in Figure 2c. Other inclusion types, such as Ti-Ca-Mn-O, Ti-Mn-O-S, and MnS, were also observed. Some nital-etched samples that were subjected to thermomechanical

simulation are also presented in Figure 3 to indicate the effective inclusion types for AF nucleation. It was seen that several AF plates emanated from the inclusion, which acted as a nucleating substrate. Bhadeshia et al. [17] have shown that a single acicular ferrite does not often have needle-like characteristics, but is lenticular. This is because it is difficult for a section specimen to be exactly on its wide surface. Figure 3a–c shows the three dominant types effective for AF nucleation in TC# steel. They can be classified as TiO_x-MnS-Al_2O_3-CaO, TiO_x-MnO-Al_2O_3-CaO, and TiO_x-MnS inclusions. For AC# steel, Al_2O_3-CaO-MnS was the dominant type and exhibited weaker AF nucleation ability in general, as shown in Figure 3d.

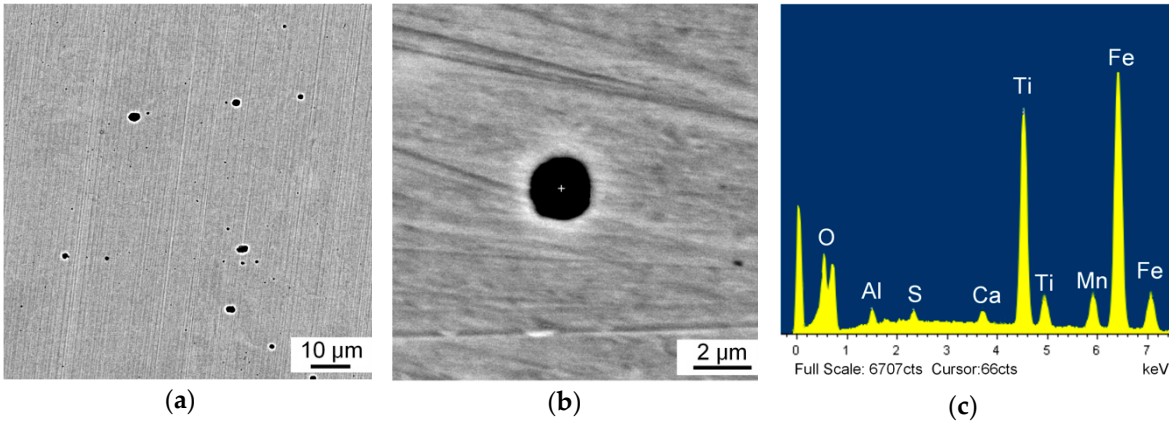


Figure 2. (**a**) An example of electron probe microanalyzer (EPMA) micrographs used for inclusion statistics; (**b**) EPMA micrograph at higher magnification; (**c**) energy dispersive spectroscopy (EDS) analysis of typical inclusion in TC# steel.

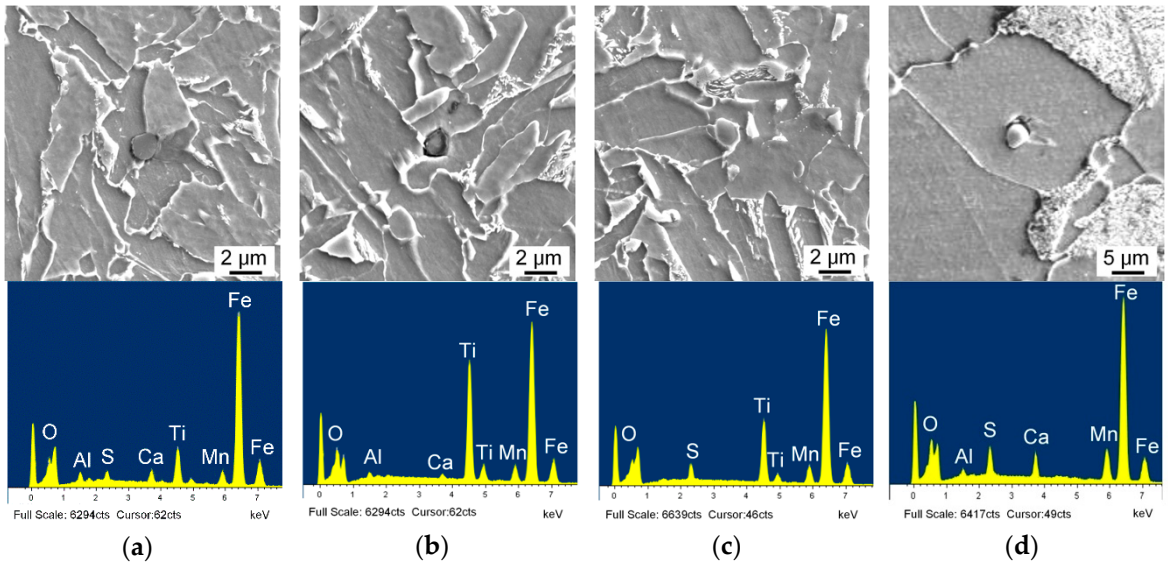


Figure 3. Typical inclusions in (**a**–**c**) TC# steel and (**d**) AC# steel.

Statistical results of inclusion number density and size distribution are shown in Figure 4. Besides the chemical composition, inclusion size is also a decisive factor affecting AF nucleation ability. Mu et al. [8] concluded that the suitable size of Ti-oxide inclusion for intragranular ferrite formation ranged from 0.45 to 2.0 μm. Inclusions of diameter <0.2 μm are ignored in Figure 4a. Inclusions in both steels were mostly less than 3 μm, and the number of fine inclusions in TC# steel was significantly higher than in AC# steel. Aluminum is a kind of strong deoxidant, and its deoxidation product becomes easily removed after Ca treatment. The frequency of different inclusion types in TC#

steel is presented in Figure 4b. The observation results showed Ti-Al-Ca-O-Mn-S complex inclusions were quite effective for AF nucleation.

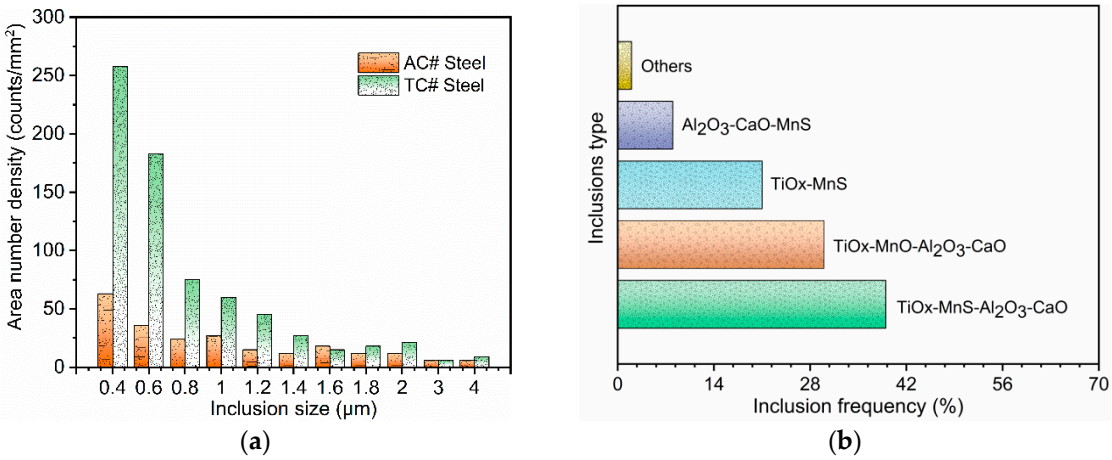


Figure 4. (**a**) Size distributions of inclusions in TC# and AC# steels; (**b**) frequency of each inclusion type in TC# steel.

3.2. Microstructural Evolution Behaviors

According to the thermomechanical simulation experiment results, continuous cooling transformation (CCT) diagrams of two steels were drawn and are shown in Figure 5. These diagrams were used to understand the microstructures presented in Figures 6–8.

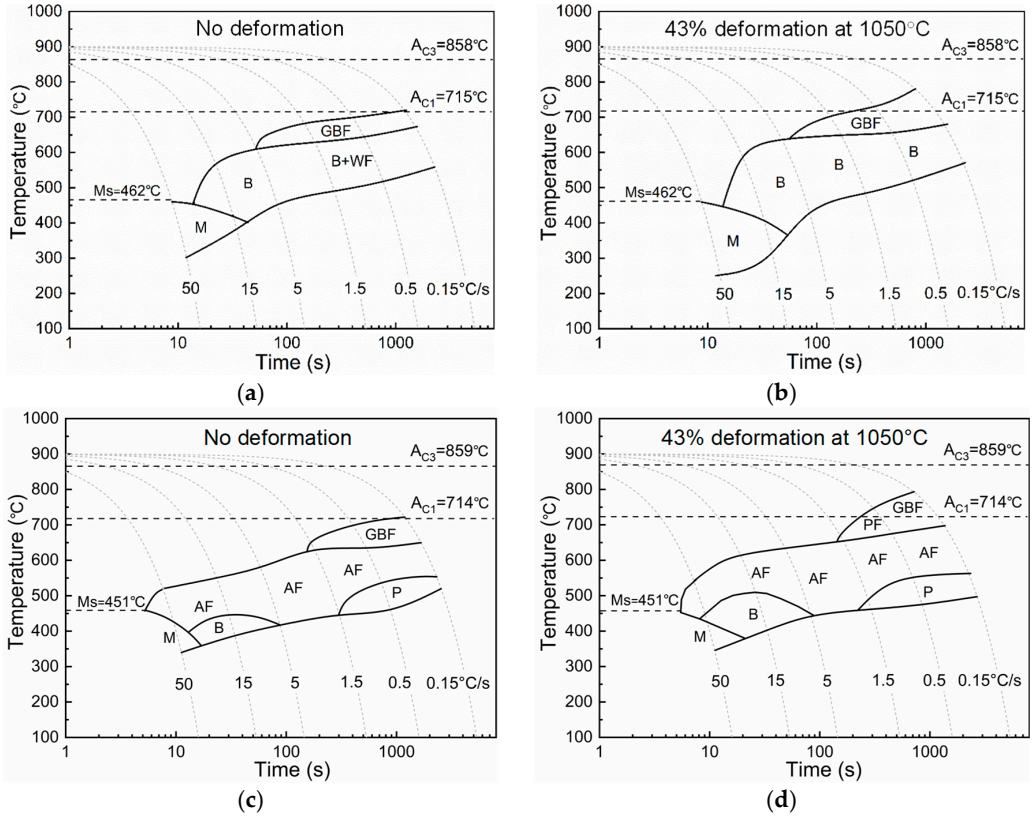


Figure 5. Continuous cooling transformation (CCT) diagrams of (**a**,**b**) AC# steel and (**c**,**d**) TC# steel. GBF: Grain boundary ferrite; WF: Widmanstätten ferrite; AF: Acicular ferrite; P: Pearlite; B: Bainite; M: Martensite.

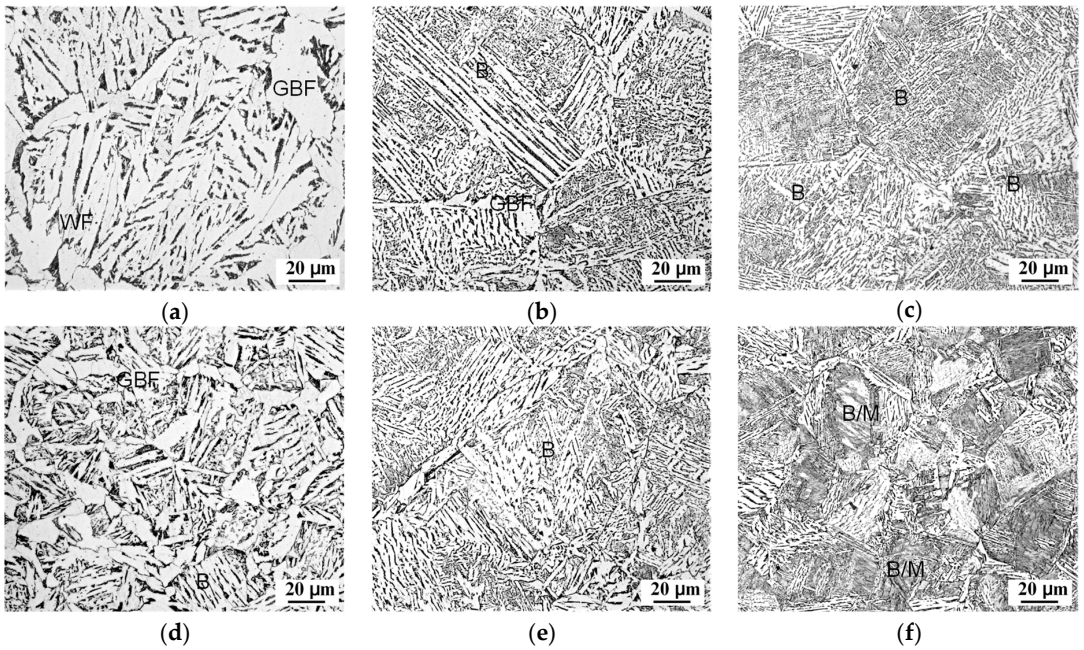


Figure 6. Microstructures of AC# steel formed at cooling rates of (**a**,**d**) 2 °C/s, (**b**,**e**) 5 °C/s, and (**c**,**f**) 15 °C/s with (**a**–**c**) no deformation and (**d**–**f**) 43% deformation at 1050 °C.

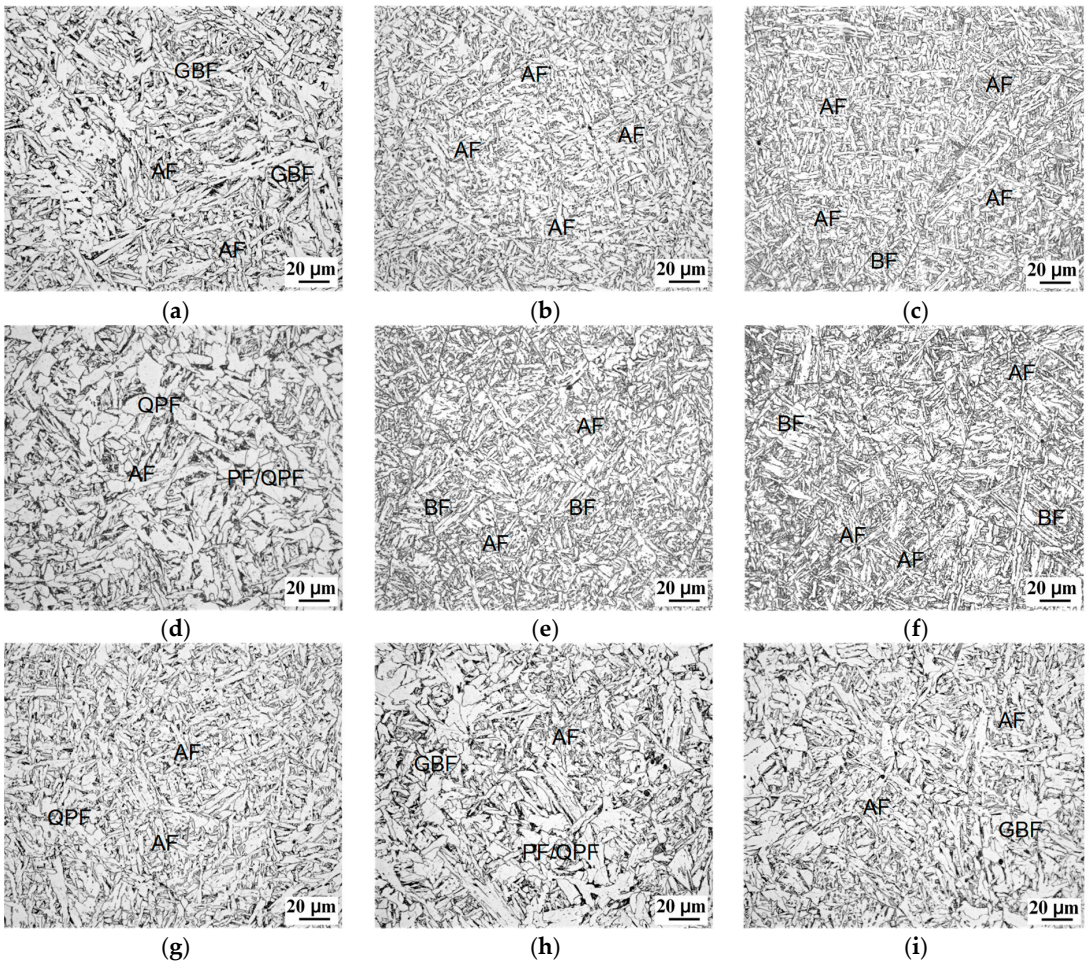


Figure 7. Microstructures of TC# steel formed at cooling rates of (**a**,**d**,**g**–**i**) 2 °C/s, (**b**,**e**) 5 °C/s, and (**c**,**f**) 15 °C/s under different deformation conditions: (**a**–**c**) No deformation; (**d**–**f**) 43%, 5 s^{-1}; (**g**) 15%, 5 s^{-1}; (**h**) 65%, 5 s^{-1}; (**i**) 43%, 3 s^{-1}, at 1050 °C.

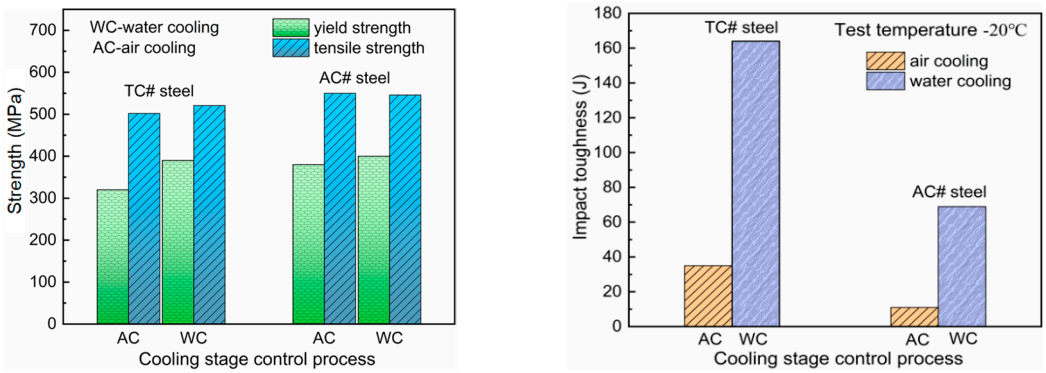


Figure 8. (**a**) Tensile and (**b**) impact properties of hot-rolled steel plates with different cooling conditions.

The microstructures of AC# steel formed at typical cooling rates with or without hot deformation are presented in Figure 6. Under the condition without deformation, Widmanstätten ferrite (WF) growing from grain boundary allotriomorphic ferrite (GBF) predominated the microstructure at the cooling rate of 2 °C/s, where quite limited intragranular AF was observed (Figure 6a). As the cooling rate increased to 5 °C/s, an upper bainite structure was mainly formed. Coarse bainite sheaves often grow across the entire austenite grain or impinge each other, as shown in Figure 6b. The microstructure formed at 15 °C/s was of a similar type to that of 5 °C/s, but the sizes of the bainite packet and the bainitic ferrite lath became much finer (Figure 6c). Under the condition with hot deformation, the microstructures formed at each cooling rate were basically similar to those without deformation. Their differences mainly consisted of three aspects. First, prior austenite grain size was apparently refined after deformation, where Nb microalloying played an important role. The resultant transformed microstructures thus became finer at each cooling rate. Second, transformation start temperatures increased after deformation, which are reflected in CCT diagrams in Figure 5a,b. Third, the volume of Widmanstätten ferrite decreased, and intragranular ferrite tended to increase, especially for the cooling rate of 2 °C/s (Figure 6d).

Figure 7 shows the microstructures of TC# steels formed under different thermomechanical simulation conditions. Figure 7a–f are microstructures without hot deformation and with the same deformation of 43% reduction, respectively. Figure 7g–i shows transformation products at the same cooling rate of 2 °C/s with different deformation parameters. The microstructural constituents described here refer to previous research on HSLA steels [18–22]. Under the condition without deformation, AF dominant microstructures were formed at a wide range of cooling rates. The main effect of an increase in the cooling rate was a decrease in AF transformation temperature and a refinement of AF lath size, as shown in Figures 5c and 7a–c. At the lower cooling rate of 2 °C/s, a small amount of GBF and quite limited WF were still formed. At 5 °C/s, an interlocking AF structure was well developed, as indicated in Figure 7b. When the cooling rate increased further, the lath size of AF was refined accordingly, and meanwhile limited bainite ferrite (BF) packets could also form, as shown in Figure 7c.

Hot deformation exhibited greater influence on transformation for TC# steel in comparison to AC# steel. The effects of deformation on TC# steel microstructures consisted of the following three aspects. First, the temperature range of phase transformation was enlarged after applying deformation, as referred to in Figure 5c,d. More microstructural constituents would form at a certain cooling rate. Second, at lower cooling rates, grain boundary or intragranular polygonal ferrite (PF) grains increased. Quasi-polygonal ferrite (QPF) grains with irregular boundaries were also included, as demonstrated in Figure 7d. Third, at higher cooling rates, bainite packets growing from austenite grain boundaries increased significantly, as indicated in Figure 7e,f. These effects mainly resulted from the increase in recrystallized austenite grain boundaries, which acted as effective nucleating sites.

Figure 7g–i shows the effects of deformation degree and strain rate. It was obviously found that a small reduction of 15% (Figure 7g) was quite favorable for AF formation compared to that of 43% (Figure 7d) and 65% (Figure 7h) under the same strain rate of 5 s^{-1} and cooling rate of 2 °C/s. The AF structure morphology was even better developed than that without deformation (Figure 7a). A proper small deformation contributed to inhibiting WF formation through reducing the coarse austenite grain size and resulted in a full AF microstructure formation. However, an excessive large deformation would cause a remarkable increase in the grain boundary reaction product. In contrast, the strain rate decreasing from 5 to 3 s^{-1} had less influence on the resultant microstructure, while AF volume tended to increase, as shown in Figure 7i.

3.3. Hot Rolling Steels

The mechanical properties of hot-rolled steels are presented in Figure 8. The corresponding microstructures are shown in Figure 9. At the low cooling rate in air, both steels obtained coarse proeutectoid ferrite grains, leading to low strength and poor impact toughness. AC# steel showed even higher strength than TC# steel as a result of precipitation strengthening by Nb microalloying. Under the condition of accelerated water cooling, the microstructure of TC# steel changed a lot and got significantly refined. The yield strength was accordingly increased by 70 MPa and, in particular, the toughness was remarkably improved by 130 J. However, accelerated cooling did not have such an important effect on microstructure refinement and property improvement of AC# steel. It is worth noting that commercial steel with the same composition as AC# steel was supposed to apply a controlled cooling technology, where austenite and the resultant ferrite would be significantly refined. However, under the high temperature rolling condition, austenite was relatively coarse, and grain refinement could only be realized through intragranular nucleation.

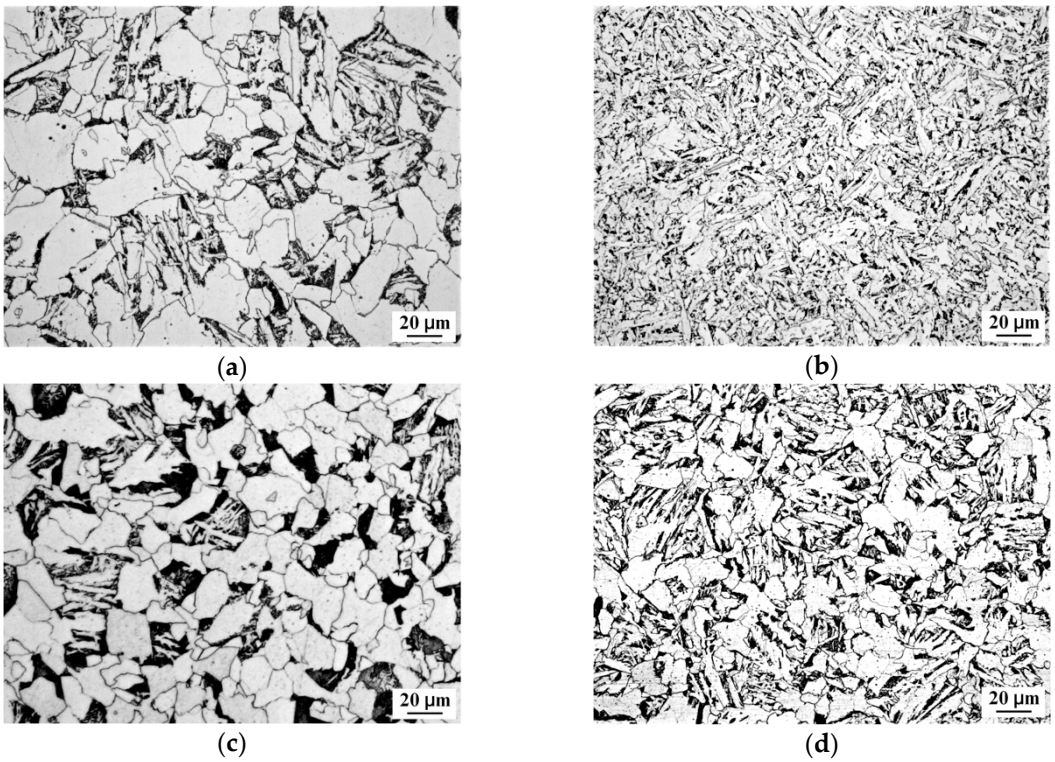
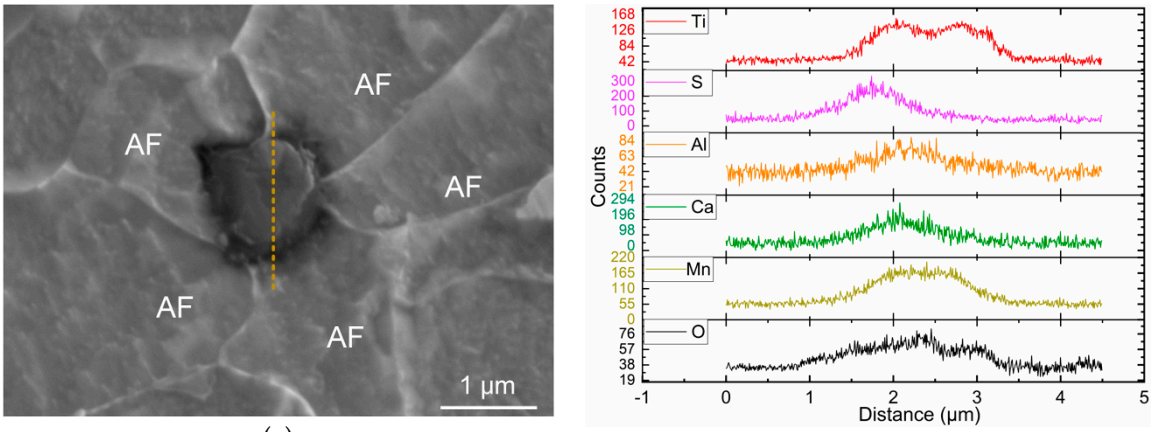


Figure 9. Microstructures of hot-rolled (**a**,**b**) TC# steel and (**c**,**d**) AC# steel with (**a**,**c**) air cooling and (**b**,**d**) accelerated water cooling conditions.

4. Discussion

4.1. Mechanism of AF Nucleation Promoted by Ti–Ca Oxide Inclusions

In previous studies, four principal mechanisms for inclusion-induced ferrite nucleation have been proposed, i.e., element depletion, lattice matching, thermal strain, and inert substrate [5,7,9]. In the present research, the mechanism is discussed by combining inclusion characterization and thermodynamic calculations. EPMA was used to detect effective oxide particles inducing AF nucleation. Composition analysis of one effective inclusion through WDS line scanning is shown in Figure 10. It indicates that the effective particle was of a Ti-Al-Ca-O-Mn-S composite type. With regard to Ti-oxide inducing AF nucleation, a previous study concluded that Mn absorption into Ti_2O_3 particles is responsible for the Mn depletion zone (MDZ) formation [23]. However, in the present work, MDZs near Ti-Al-Ca-O-Mn-S particles were not found under the resolution. This does not seem to indicate that MDZs did not exist. Because the formation of an MDZ is a dynamic atomic diffusion process with a small distance [24], it is difficult to detect the concentration gradient of an MDZ by the conventional WDS analysis method.



(**a**) (**b**)

Figure 10. (**a**) EPMA micrograph of an inclusion nucleating AF in TC# steel and (**b**) line scanning analysis across the inclusion by wavelength dispersive spectroscopy (WDS).

In order to evaluate the effect of Mn content on austenite-ferrite transformation, the start temperature and driving force for ferrite formation were calculated by Thermo-Calc software, with the results presented in Figure 11. An increase in Mn concentration could lead to a decrease in $\gamma \rightarrow \alpha$ start temperature, which could inhibit the formation of grain boundary ferrite and intragranular ferrite simultaneously. The formation of MDZ caused a decrease in Mn content and an increase in transformation temperature, which promoted intragranular AF nucleation around the inclusion. Moreover, the driving force for ferrite formation, i.e., the Gibbs free energy change, increased with a decrease in Mn content, which contributed to promoting AF nucleation. In addition, the driving force for the transformation from austenite to ferrite significantly increased with a decrease in temperature, as shown in Figure 11b. At a higher cooling rate, the formation temperature of AF was lower, as indicated in Figure 12, which would generate a higher driving force for ferrite formation. Under this condition, the AF nucleation rate increased, and a much finer AF dominant microstructure was formed (refer to Figure 7).

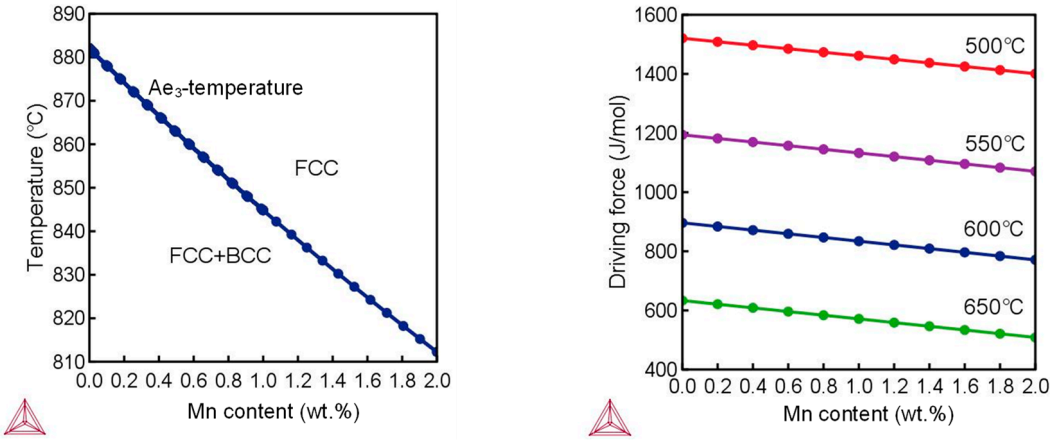


Figure 11. Effect of Mn on the kinetics of transformation calculated by Thermo-Calc. (**a**) Relationship between Ae_3-temperature and Mn content; (**b**) ferrite formation driving force at different temperatures.

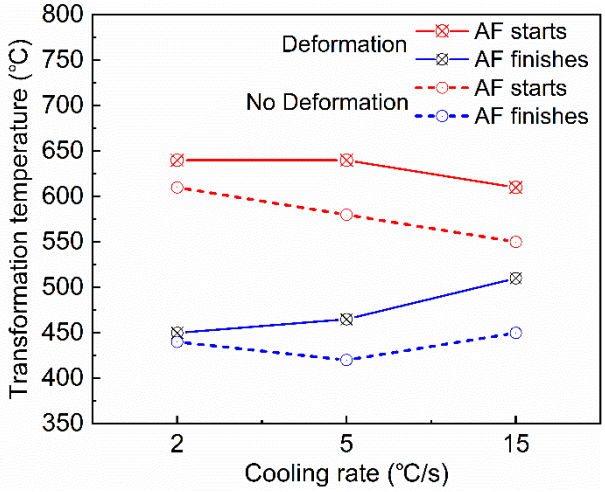


Figure 12. Effect of cooling rate on formation temperature of AF in TC# steel.

4.2. EBSD Interpretation of AF Microstructure

AF microstructures of TC# steel obtained under different thermomechanical conditions were further analyzed by EBSD technology. Figure 13 is an EBSD inverse pole figure (IPF) map of the steel sample subjected to a 43% deformation and 5 °C/s continuous cooling (the same sample as Figure 7e). The three main microstructural constituents, i.e., BF, QPF, and AF, are indicated in Figure 13a, and the corresponding SEM morphologies are presented in Figure 13b–d, respectively. Here, BF, QPF, and AF could be identified by parallel lath packets, irregular grain boundaries, and interlocking ferrite plates, respectively. Obviously, the interlocking AF plates had different crystallographic orientations and high-angled grain boundaries (HAGBs), while the parallel bainite ferrite laths were of a similar orientation. Crystallographic grain boundaries with a misorientation angle >15° acted as obstacles to crack propagation and increased the absorbed energy.

Figure 14 shows EBSD maps of TC# samples with different cooling rates. It is clearly observed that PF/QPF had high-angled grain boundaries. Both acicular ferrite and bainite packet boundaries were HAGBs. Figure 15 shows that the misorientation angle distribution exhibited a "double-peak" feature with an absence of boundary angles between 21° and 47°. In bainitic transformation, the bainitic ferrite keeps a K–S and/or N–W relationship with the parent austenite [25,26]. The acicular ferrite transformation mechanism is similar to bainite, so there must be a specific orientation difference between the ferrite plates transformed from the parent phase in a specific orientation

relationship. The difference in orientation between the variants of the relationship is concentrated in 2–20° and 48–65° intervals. From Figure 15, it can be seen that the HAGB fraction of the sample cooled at 5 °C/s was the highest because of full AF structure formation. Moreover, PF/QPF in deformed samples and bainite formed at a high cooling rate both caused a decrease in HAGBs. Besides, the crystallographic grain sizes were measured using an image-quality map containing grain boundaries with a misorientation angle >15°. The mean sizes of the sample with cooling rates of 2, 5, and 15 °C/s were 24.2, 13.3, and 17.2 μm, respectively. Crystallographic grain size was considered to be the effective grain size and corresponded to the cleavage facet size developed in a brittle fracture surface. The result indicated that a fine crystallographic grain size under a cooling rate of 5–15 °C/s would lead to high impact toughness.

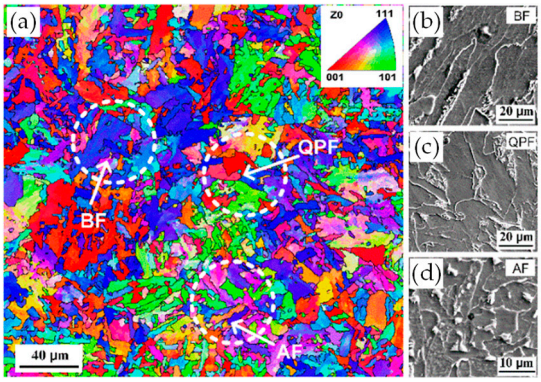


Figure 13. (**a**) Electron backscattered diffraction (EBSD) inverse pole figure (IPF) map and (**b**–**d**) corresponding SEM micrographs of different constituents of the TC# steel sample subjected to 43% deformation and 5 °C/s cooling.

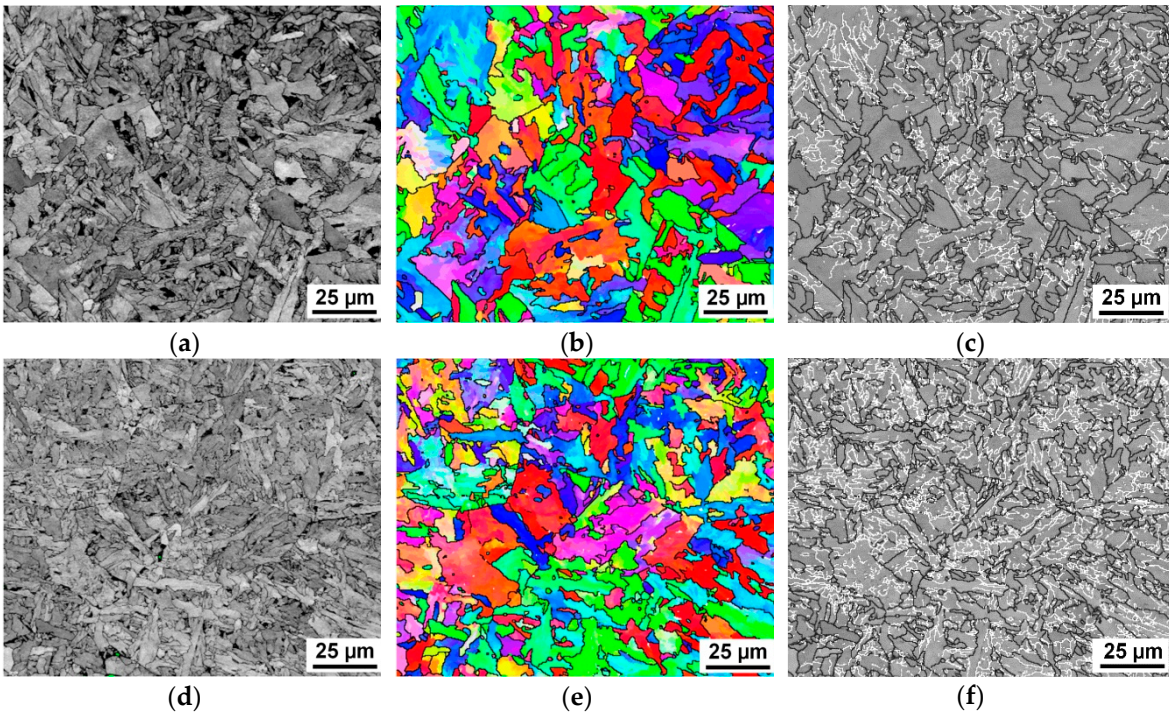


Figure 14. *Cont.*

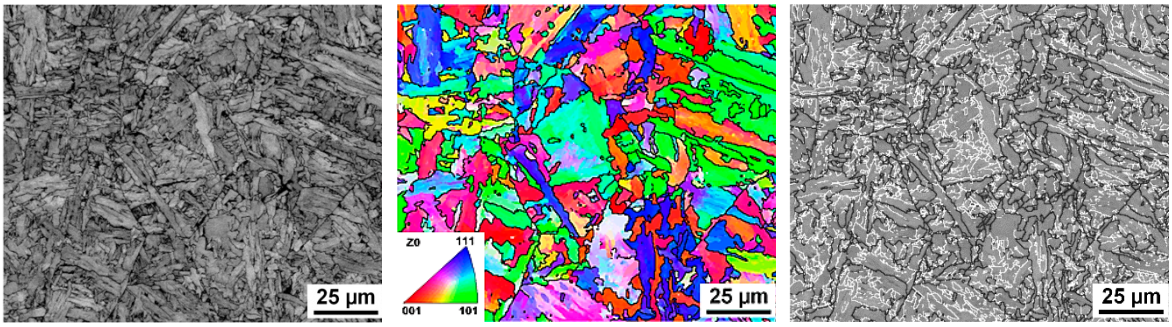


Figure 14. EBSD maps of TC# samples with deformation and cooling rates of (**a**–**c**) 2 °C/s, (**d**–**f**) 5 °C/s, and (**g**–**i**) 15 °C/s. (**a**,**d**,**g**) Image quality maps; (**b**,**e**,**h**) inverse pole figure maps; (**c**,**f**,**i**) grain boundaries of misorientation angle >15° (black) and 2–15° (blue).

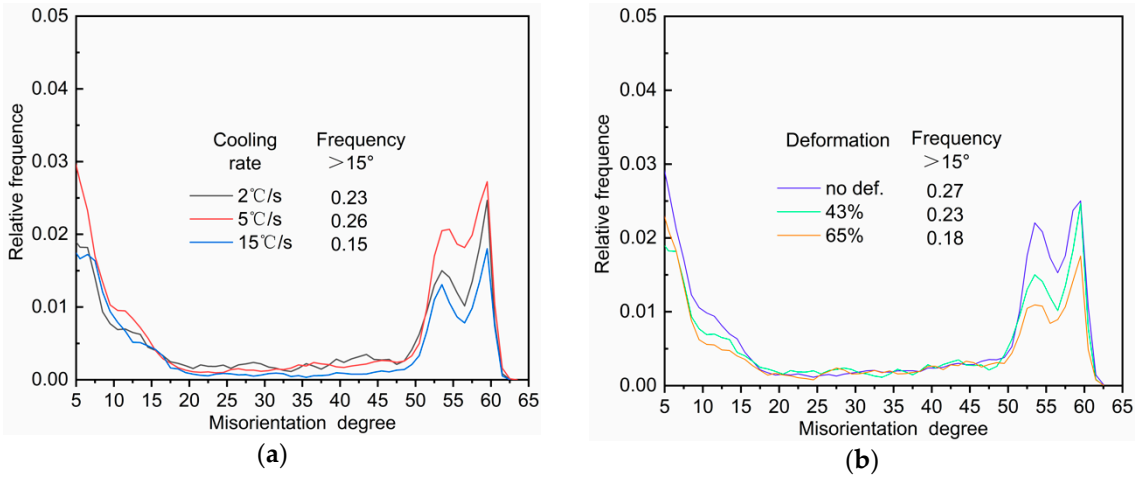


Figure 15. Grain boundary misorientation angle distribution in TC# steel samples under different thermomechanical treatment conditions.

In summary, AF showed similar transformation behaviors and microstructure characteristics to those of bainite. Therefore, it is reasonable to say that the AF transformation mechanism was in fact bainitic, which is also agreed with by many other researchers [27–29]. A suitable rolling deformation and cooling process can be used to improve the proportion of HAGBs, which is of great significance for engineering applications, especially in terms of impact toughness.

4.3. Process–Microstructure–Hardness Relationship

The bainitic-type growth of the AF plate is restricted within one prior austenite grain because the coordinated motion of atoms cannot be sustained across an arbitrary grain boundary [29,30]. In addition, the acicular ferrite keeps a well-defined crystallographic orientation relationship with austenite. Therefore, the transformation to acicular ferrite was expected to be affected by thermomechanical treatment of austenite. Accordingly, mechanical properties would be thus influenced. Here, the hardness of the thermomechanical simulation samples was used to reflect the relationship between microstructure and properties. Microhardness test results of TC# steel showed that the value of PF/QPF was between 138 and 160, and the value of AF was between 170 and 215. Previous research has indicated microhardness values of PF and BF were HV140 and HV220, respectively, and AF had a similar strength to BF [31,32]. Macrohardness was then tested to accurately understand the effects of different process parameters. The results are presented in Figure 16.

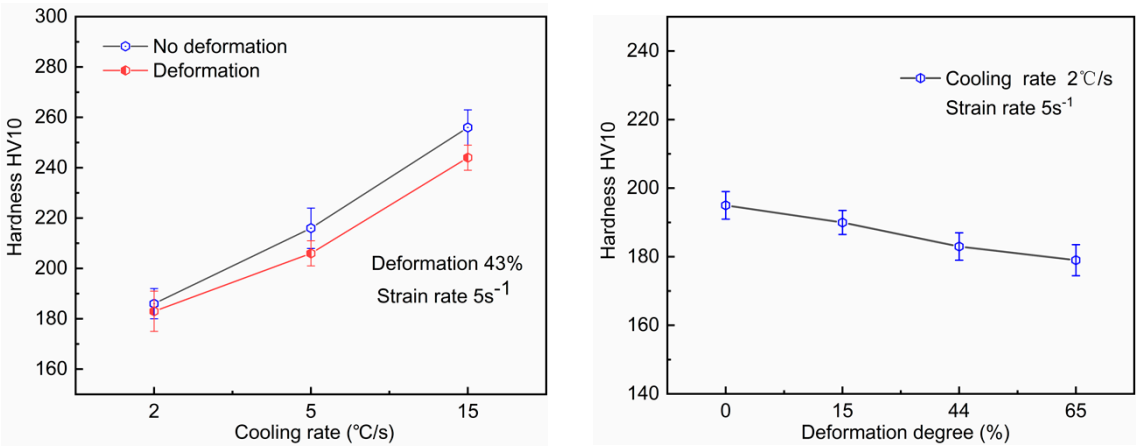


Figure 16. Effects of deformation (**a**) and cooling rate (**b**) on the macrohardness of TC# steel.

Figure 16 shows the hardness variation with deformation degree and cooling rate. On the whole, hardness increased as cooling rate increased from 2 °C/s to 15 °C/s, and the hardness of deformed samples was lower than without deformation. The PF/QPF constituents accounted for a considerable part at 2 °C/s, especially for deformed samples. With the cooling rate increasing to 5 °C/s, the hardness value increased obviously because PF/QPF was inhibited and an almost full AF structure was formed. At a cooling rate up to 15 °C/s, the hardness increased further because the AF forming at a lower temperature had a higher dislocation density and bainite packets also increased.

Figure 16b shows that a small amount of austenite deformation (15%) had little influence on transformation and hardness. As the deformation increased, GBF and PF/QPF improved so that the hardness was accordingly reduced. With the adopted large hot deformation, prior austenite grain was refined through recrystallization, and nucleating sites on the grain boundary increased, which resulted in an increase in GBF and a decrease in AF. The results indicated that suitable rolling deformation and accelerated cooling can significantly improve acicular ferrite formation and steel performance.

5. Conclusions

Acicular ferrite transformation in low-carbon steel under thermomechanical treatment conditions was studied. The main conclusions are as follows:

(1) Inclusions in Ti–Ca deoxidized steel were mainly of a Ti-Al-Ca-O-Mn-S composite type. The observed typical inclusions TiO_x-MnS-Al_2O_3-CaO, TiO_x-MnO-Al_2O_3-CaO, and TiO_x-MnS were effective for intragranular acicular ferrite nucleation and responsible for microstructure refinement. The Mn-depletion zone mechanism was applicable to the present steel;

(2) An increase in the cooling rate up to 15 °C/s could inhibit the grain boundary reaction product and reduce transformation temperature. The driving force for transformation from austenite to ferrite increased at lower temperatures, resulting in fine AF dominant microstructure formation. However, a high deformation of 43–65% discouraged the formation of full acicular ferrite microstructures because of the increase in austenite grain boundaries serving as nucleation sites.

(3) High-angled grain boundaries acted as obstacles to cleavage crack propagation and improved toughness. The HAGB fraction of the sample cooled at 5 °C/s was the highest because of full AF structure formation. The grain boundary misorientation angle distribution of the AF structure exhibited a "double-peak" feature, which was similar to bainite transformation.

(4) The hardness increased significantly as the cooling rate increased from 2 to 15 °C/s, while it decreased under the condition of deformation because of the formation of (quasi-)polygonal ferrite. By applying accelerated water cooling, the mechanical properties, particularly impact toughness, were significantly improved as a result of fine AF microstructure formation.

Author Contributions: Funding acquisition, C.W. and G.Y.; investigation, C.W. and X.W.; methodology, J.K. and G.Y.; supervision, G.W.; writing—original draft, C.W. and X.W.; writing—review and editing, J.K. and G.Y.

Funding: This research was funded by the National Natural Science Foundation of China (grant number U1860201), the China Postdoctoral Science Foundation (grant number 2018M631804), and the Fundamental Research Funds for the Central Universities (grant number N170703005).

Conflicts of Interest: The authors declare no conflicts of interest.

References

1. Takamura, J.; Mizoguchi, S. Roles of oxides in steels performance–metallurgy of oxides in steels. In Proceedings of the 6th International Iron and Steel Congress, Nagoya, Japan, 21–26 October 1990.
2. Min, Y.; Li, X.B.; Yu, Z.; Liu, C.L.; Jiang, M.F. Characterization of the acicular ferrite in Al-deoxidized low-carbon steel combined with Zr and Mg additions. *Steel Res. Int.* **2016**, *87*, 1503–1510. [CrossRef]
3. Loder, D.; Michelic, S.K. Systematic investigation of acicular ferrite formation on laboratory scale. *Mater. Sci. Technol.* **2017**, *33*, 162–171. [CrossRef]
4. Ilman, M.N.; Cochrane, R.C.; Evans, G.M. The development of acicular ferrite in reheated Ti–B–Al–N-type steel weld metals containing various levels of aluminium and nitrogen. *Weld. World* **2015**, *59*, 565–575. [CrossRef]
5. Mu, W.; Mao, H.; Jönsson, P.G.; Nakajima, K. Effect of carbon content on the potency of the intragranular ferrite formation. *Steel Res. Int.* **2016**, *87*, 311–319. [CrossRef]
6. Capdevila, C.; García-Mateo, C.; Chao, J.; Caballero, F.G. Effect of V and N precipitation on acicular ferrite formation in sulfur-lean vanadium steels. *Metall. Mater. Trans. A* **2009**, *40A*, 522–538. [CrossRef]
7. Sarma, D.S.; Karasev, A.V.; Jönsson, P.G. On the role of non-metallic inclusions in the nucleation of acicular ferrite in steels. *ISIJ Int.* **2009**, *49*, 1063–1074. [CrossRef]
8. Mu, W.; Jönsson, P.G.; Nakajima, K. Recent aspects on the effect of inclusion characteristics on the intragranular ferrite formation in low alloy steels: a review. *High Temp. Mater. Processes* **2017**, *36*, 1–17. [CrossRef]
9. Loder, D.; Michelic, S.K.; Bernhard, C. Acicular ferrite formation and its influencing factors-a review. *J. Mater. Sci. Res.* **2017**, *6*, 24–43. [CrossRef]
10. Li, X.; Min, Y.; Liu, C.; Jiang, M.F. Study on the formation of intragranular acicular ferrite in a Zr-Mg-Al deoxidized low carbon steel. *Steel Res. Int.* **2016**, *87*, 622–632. [CrossRef]
11. Hui, K.; Shao, S.; Shen, Y.F.; Yan, Y.H.; Qiang, Y.; Zang, J.F.; Cai, Z.Y. Effect of aluminum on the nucleation of intragranular ferrite in Ti-added carbon structural steel. *High Temp. Mater. Processes* **2013**, *32*, 323–329. [CrossRef]
12. Mu, W.; Jönsson, P.G.; Shibata, H.; Nakajima, K. Inclusion and microstructure characteristics in steels with TiN additions. *Steel Res. Int.* **2016**, *87*, 339–348. [CrossRef]
13. Wang, C.; Wang, Z.; Wang, G. Effect of hot deformation and controlled cooling process on microstructures of Ti-Zr deoxidized low carbon steel. *ISIJ Int.* **2016**, *56*, 1800–1807. [CrossRef]
14. Huang, Q.; Wang, X.; Jiang, M.; Hu, Z.Y.; Yang, C.W. Effects of Ti-Al complex deoxidization inclusions on nucleation of intragranular acicular ferrite in C-Mn steel. *Steel Res. Int.* **2016**, *87*, 445–455. [CrossRef]
15. Kang, Y.; Jeong, S.; Kang, J.H.; Lee, C. Factors affecting the inclusion potency for acicular ferrite nucleation in high-strength steel welds. *Metall. Mater. Trans. A* **2016**, *47A*, 2842–2854. [CrossRef]
16. Boratto, F.; Barbosa, R.; Yue, S.; Jonas, J.J. Effect of chemical composition on the critical temperature of microalloyed steels. In Proceedings of the International Conference on Physical Metallurgy of Thermomechanical Processing of Steels and Other Metals (THERMEC-88), Tokyo, Japan, 6–10 June 1988; Tamura, I., Ed.; ISIJ: Tokyo, Japan, 1988.
17. Bhadeshia, H.K.D.H. *Bainite in Steels*, 2nd ed.; IOM Communication Ltd.: London, UK, 2001; pp. 101–106.
18. Krauss, G.; Thompson, S.W. Ferritic microstructures in continuously cooled low-and ultralow-carbon steels. *ISIJ Int.* **1995**, *35*, 937–945. [CrossRef]
19. Bhadeshia, H.K.D.H. Developments in martensitic and bainitic steels: role of the shape deformation. *Mater. Sci. Eng. A* **2004**, *378*, 34–39. [CrossRef]
20. Van Bohemen, S.M.C.V.; Sietsma, J. The kinetics of bainite and martensite formation in steels during cooling. *Mater. Sci. Eng. A* **2010**, *527*, 6672–6676. [CrossRef]

21. Zhu, K.; Chen, H.; Masse, J.P.; Bouzaiz, O.; Gacheta, G. The effect of prior ferrite formation on bainite and martensite transformation kinetics in advanced high-strength steels. *Acta Mater.* **2013**, *61*, 6025–6036. [CrossRef]
22. Kang, H.C.; Park, B.J.; Jang, J.H.; Jang, K.S.; Lee, K.J. Determination of the continuous cooling transformation diagram of a high strength low alloyed steel. *Met. Mater. Int.* **2016**, *22*, 949–955. [CrossRef]
23. Seo, K.; Kim, Y.M.; Evans, G.M.; Kim, H.J.; Lee, C. Formation of Mn-depleted zone in Ti-containing weld metals. *Weld. World* **2015**, *59*, 373–380. [CrossRef]
24. Byun, J.S.; Shim, J.H.; Cho, Y.W.; Lee, D.N. Non-metallic inclusion and intragranular nucleation of ferrite in Ti-killed C–Mn steel. *Acta Mater.* **2003**, *51*, 1593–1606. [CrossRef]
25. Cabus, C.; Réglé, H.; Bacroix, B. Orientation relationship between austenite and bainite in a multiphased steel. *Mater. Charact.* **2007**, *58*, 332–338. [CrossRef]
26. Caballero, F.G.; Yen, H.W.; Miller, M.K.; Yang, J.R.; Cornidea, J.; Garcia-Mateoa, C. Complementary use of transmission electron microscopy and atom probe tomography for the examination of plastic accommodation in nanocrystalline bainitic steels. *Acta Mater.* **2011**, *59*, 6117–6123. [CrossRef]
27. Yang, J.R.; Huang, C.Y.; Huang, C.F.; Aoh, J.N. Influence of acicular ferrite and bainite microstructures on toughness for an ultra-low-carbon alloy steel weld metal. *J. Mater. Sci. Lett.* **1993**, *12*, 1290–1293. [CrossRef]
28. Wan, X.L.; Wu, K.M.; Huang, G.; Wei, R. In situ observations of the formation of fine-grained mixed microstructures of acicular ferrite and bainite in the simulated coarse-grained heated-affected zone. *Steel Res. Int.* **2014**, *85*, 243–250. [CrossRef]
29. Bhadeshia, H.K.D.H.; Christian, J.W. Bainite in steels. *Metal. Mater. Trans.* **1990**, *21A*, 767–797. [CrossRef]
30. Gourgues, A.F.; Flower, H.M.; Lindley, T.C. Electron backscattering diffraction study of acicular ferrite, bainite, and martensite steel microstructures. *J. Mater. Sci. Technol.* **2000**, *16*, 26–40. [CrossRef]
31. Shibata, K.; Asakura, K. Transformation behavior and microstructures in ultra-low carbon steels. *ISIJ Int.* **1995**, *35*, 982–991. [CrossRef]
32. Zhao, H.; Palmiere, E.J. Effect of austenite deformation on the microstructure evolution and grain refinement under accelerated cooling conditions. *Metall. Mater. Trans. A* **2017**, *48*, 3389–3399. [CrossRef]



© 2019 by the authors. Licensee MDPI, Basel, Switzerland. This article is an open access article distributed under the terms and conditions of the Creative Commons Attribution (CC BY) license (http://creativecommons.org/licenses/by/4.0/).